Modelling the dynamics of hydrogen synthesis from methane in nanosecond-pulsed plasmas

Eduardo Morais and Annemie Bogaerts

PLASMANT, Department of Chemistry, University of Antwerp, Antwerp 2610, Belgium

Correspondence:
Annemie Bogaerts, annemie.bogaerts@uantwerpen.be
Eduardo Morais, eduardo.morais@uantwerpen.be

PLASMANT, Department of Chemistry, University of Antwerp, Campus Drie Eiken, Antwerp 2610, Belgium

Abstract

A chemical kinetics model was developed to characterise the gas-phase dynamics of H_2 production in nanosecond-pulsed CH_4 plasmas. Pulsed behaviour was observed in the calculated electric field, electron temperature and species densities at all pressures. The model agrees reasonably with experimental results, showing CH_4 conversion at 30% and C_2H_2 and H_2 as major products. The underlying mechanisms in CH_4 dissociation and H_2 formation were analysed, highlighting the large contribution of vibrationally excited CH_4 and H_2 to coupling energy from the plasma into gas-phase heating, and revealing that H_2 synthesis is not affected by applied pressure, with selectivity remaining unchanged at ~ 42% in the 1 to 5 bar range.

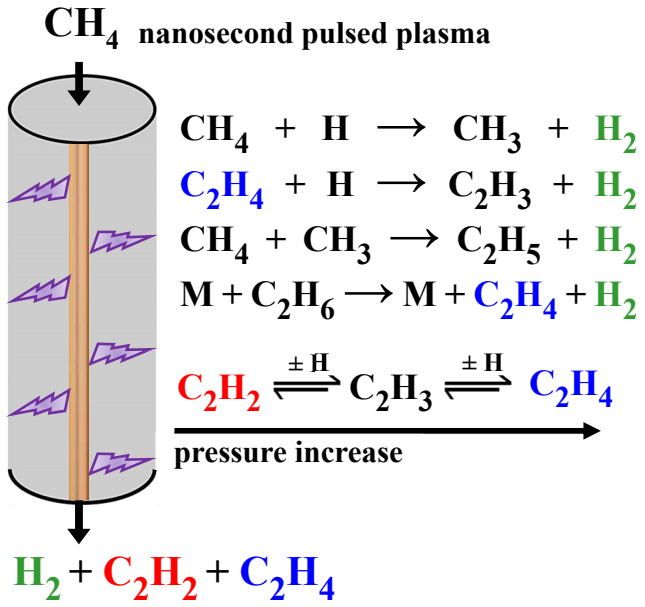

Keywords

Hydrogen; chemical kinetics model; nanosecond pulsed discharges; methane; reaction mechanism

1. Introduction

As society turns away from finite and non-renewable fossil fuel resources, hydrogen production (for numerous applications) becomes a critical research subject within the efforts to remodel the framework for energy generation. Sustainable and efficient CO_2-free H_2 production can be accomplished by plasma-based CH_4 conversion [1]–[4]. The clear advantage of employing plasma technology in this process is related with the ease to avail of the current renewable energy infrastructure (i.e. solar, hydroelectric, wind, etc.) to promote CH_4 dissociation and conversion [3]–[5]. In turn, plasma can forgo indirect CO_2 emissions from the traditional fossil-fuel-based energy sources currently applied in CH_4 reforming for reactor heating [6], resulting in a fully circular carbon process.

Even though the utilisation of plasma in CH_4 reforming is in rapid expansion, there is a gap to be bridged between plasma-assisted CH_4 conversion and conventional processes in terms of operating efficiency and stability, selectivity and addition of catalysts [3], [7]. A variety of plasma reactors (in the thermal, warm and non-thermal plasma regimes) has been tested in CH_4 reforming [2]–[4], [8], [9], each yielding significantly different CH_4 conversions and product selectivity, mainly depending on the electron and gas temperature [4], [8]. Generally, warm plasmas, such as microwave and gliding arc plasmas, are preferred for H_2 generation, as the gas temperature (in the range of a few 1000 K) favours dehydrogenation of C_xH_y species, directing the selectivity towards $C_{(s)}$ and C_2H_2 (and consequently H_2) [1], [2], [10].

More recently, the utilisation of nanosecond pulsed discharges (NPD) in CH_4 conversion has been reported with considerably high CH_4 conversion (between 40 and 50%) and varying C_2H_2, C_2H_4 and C_2H_6 product distribution [11]–[13]. The versatile selectivity observed in NPD plasmas is attributed to the low degree of thermal equilibrium in pulsed plasma environments, which is ideal for applications in gas conversion, as the reactions can be driven towards specific products by changing the pulse frequency, input power and applied pressure [11], [14]–[16]. Concerning H_2 generation from CH_4 streams treated with pulsed plasmas, the mechanism of H_2 synthesis in the non-oxidative CH_4 conversion (NOMC) has not yet been elucidated and the influence of pressure on the gas-phase H_2 formation and dissociation dynamics remains unexplored [8], leaving questions about optimal operational conditions and posing difficulties to potential industrial applications [1].

This work aims to model in zero dimensions the gas-phase kinetics of an NPD CH_4 plasma to shed light on the reaction pathways of CH_4 dissociation and those of H_2 generation, consumption and (de)excitation, as well as clarify the role of applied pressure in these processes. The model also considers the vibrational excitation and relaxation kinetics of CH_4 and H_2, demonstrating how these are intimately related to gas-phase heating following the pulsed plasma discharges.

2. Description of the plasma chemical kinetics model

2.1. Numerical details

The zero-dimensional chemical kinetics model was constructed using the ZDPlasKin kinetic solver which evaluates the continuity differential equations for all chemical species p considered in the model with number density $n_p(t)$.

$$\frac{\mathrm{d}n_p}{\mathrm{d}t} = \sum_r C_{r,p}\, k_r \prod_q n_q \qquad (1)$$

where $C_{r,p}$ is the stoichiometric coefficient of a given species p in reaction r, k_r is the rate coefficient of reaction r and q is the colliding species in this process. Reactions which do not involve electron collisions have their rate coefficients k_r retrieved from the literature. k_r is often given within a temperature range and written as a function of gas temperature. In the case of electron impact reactions, k_r is extracted from continuous evaluation of collisional cross sections and the electron energy distribution function (EEDF) via the BOLSIG+ solver. BOLSIG+ operates in tandem with ZDPlasKin and requires the electric field and mean electron energy (provided by the EEDF) as inputs to return rate coefficients for electron impact reactions. ZDPlasKin was also utilised to self-consistently calculate the gas temperature as a function of time via the variation in the reaction enthalpies included in the model [17]. The model assumes that T_{gas} (in Kelvin) is identical for all neutral species, solving the adiabatic isometric heat transport equation with time [18]:

$$\frac{dT_{gas}}{dt} = (P_{e,el} + \sum_j R_j\, \Delta H_j - P_{ext}) \,/\, (N\, \frac{\gamma k}{\gamma - 1}) \qquad (2)$$

where $N = \sum n_i$ is the total neutral species density, γ is the specific heat ratio of the total gas mixture, k is the Boltzmann constant (in J K^{-1}), $P_{e,el}$ is the gas heating power density due to elastic electron-neutral collisions (in W m^{-3}), R_j is the rate of reaction j (in m^{-3} s^{-1}), ΔH_j is the heat released (or consumed when this value is negative) by reaction j (in J) and P_{ext} is the heat loss due to energy exchange with the surroundings (in W m^{-3}). The latter is given by the equation:

$$P_{ext} = \frac{8\lambda_{CH_4}}{r^2} \left(T_{gas} - T_{gas,edge}\right) \qquad (3)$$

With r being the radius of the plasma zone, T_{gas} the plasma gas temperature and $T_{gas,edge}$ the gas temperature at the edge of the plasma zone, which is assumed to be the average between room temperature and the plasma temperature, according to Berthelot [19]. The gas thermal conductivity of CH_4, λ (in W cm^{-1} K^{-1}), was taken from Hepburn et al.[20] and can be expressed as:

$$\lambda_{CH_4} = (1.49\ x\ 10^{-6}) * T_{gas} - 9.92\ x\ 10^{-5} \quad (4)$$

It should be noted that this model investigates the gas temperature in the plasma volume confined within the reactor (a finite element volume) by evaluating the reaction enthalpy of all the chemical reactions considered. It does not account for convective heat transfer since the gas flow is not included in the temperature calculations. Thus, the gas temperatures in the model may not reflect the gas temperature in the whole reactor body. More details about ZDPlasKin and BOLSIG+ can be found in [18], [21].

2.2. Chemistry component

The species included in the model are shown in Table 1. Electron impact and recombination reactions for all species were considered in this study. For a complete list of the reactions and corresponding rate coefficients (including interactions between vibrational levels), as well as relevant citations, we refer to our previous work [16], where we studied the generation of olefins from CH_4/H_2 NPD plasmas in experiments and via 0D modelling, highlighting the effect of pressure on C_2H_4 production.

Table 1. Species considered in the model.

Stable molecules	Radicals	Ions and electrons	Excited molecules
CH_4 H_2 C_2H_2 C_2H_4 C_2H_6 C_3H_6 C_3H_8 C_4H_{10} $C_{(s)}$	C C_2 C_3 H CH_3 CH_2 CH C2H C_2H_3 C_2H_5 C_3H_5 C_3H_7 C_4H_9	H^+ H_2^+ H_3^+ C^+ C_2^+ CH^+ CH_2^+ CH_3^+ CH_4^+ CH_5^+ C_2H^+ $C_2H_2^+$ $C_2H_3^+$ $C_2H_4^+$ $C_2H_5^+$ $C_2H_6^+$ H^- CH^- CH_2^- electrons	Vibrational: H_2 (v = 1…14) CH_4 (v = 1…4) Electronic: H_2* and CH_4*

2.3. Power input and number of pulses

The model was developed to investigate the results from CH_4 conversion experiments using a NPD source (n-PS, NPG-18/100k, Megaimpulse Ltd.) carried out in a coaxial configuration with a length of 25 cm and a plasma gap of 4.2 cm (the radii of the inner and outer electrode are 1.0 and 5.2 cm, respectively). The details related to reactor geometry, laboratory apparatus and experimental conditions are described in [22], [23]. In order to mimic the experimental conditions, the following parameters were applied in the model: a gas feed composition of 100% CH_4, flow rate of 200 sccm, pulse frequency of 3 kHz, residence time of 27.8 ms (i.e. time spent by the gas in the reactor) and volume of the plasma region as ~ 2% of the total reactor volume. The plasma volume was estimated considering that the diameter of an NPD streamer (taken as a column) is ~ 0.3 mm at the operating conditions [24], and the total effective reactor volume is the space defined by the NPD diameter and the plasma reactor cross-section area. Since the NPD streamer is randomly ignited around the HV electrode, the plasma volume is assumed to be equal to the total effective reactor volume occupied by each NPD event, which is approximately 2%. The number of pulses in the simulations was adjusted by multiplying the total number of pulses in the residence time by the percentage plasma

volume, which resulted in 16.7 pulses. This was then rounded to a constant number of 15 modelled pulses (i.e. molecules traversing the reactor experience one pulse every 1.9 ms, as shown in Figure 1), which is sufficient to drive this plasma system to steady state.

Power density was inserted into the model using the approach described in our previous work [16], where the power profile of pulses, and the current and voltage traces (at each studied pressure) can be found. In accordance with experimental observations [22], [25], the present work considers the pressure effect on the power density, i.e. the energy discharged by the pulses is lowered upon increasing pressure (as pulse duration is shortened), and the power pulses were constructed as asymmetrical triangles with shorter upslopes and longer downslopes.

2.4. Conversion and selectivity

The equations used to calculate experimental and modelled CH_4 conversion, and hydrocarbon and H_2 selectivity are as follows:

$$\chi_{CH_4}(\%) = 1 - \frac{n_{CH_4 f}\,(cm^{-3}) * v_f\,(cm\,s^{-1})}{n_{CH_4 i}\,(cm^{-3}) * v_i\,(cm\,s^{-1})}\,x\,100\% \quad (6)$$

$$S_{C_xH_y}(\%) = \frac{x\,n_{C_xH_y}(cm^{-3}) * v_f\,(cm\,s^{-1})}{n_{CH_4\,i}\,(cm^{-3}) * v_i(cm\,s^{-1}) - n_{CH_4 f}\,(cm^{-3}) * v_f\,(cm\,s^{-1})}\,x\,100\% \quad (7)$$

$$S_{H_2}(\%) = \frac{\frac{1}{2} * n_{H_2}(cm^{-3}) * v_f\,(cm\,s^{-1})}{n_{CH_4\,i}\,(cm^{-3}) * v_i(cm\,s^{-1}) - n_{CH_4 f}\,(cm^{-3}) * v_f\,(cm\,s^{-1})}\,x\,100\% \quad (8)$$

where n_{CH4f} and v_f are the CH_4 density and velocity at steady state, n_{CH4i} and v_i are the initial CH_4 density and velocity, and n_{CxHy} and n_{H2} are the densities of any hydrocarbon and H_2 in the steady state, respectively. The velocity (given by the flow rate divided by the cross sectional area of the reactor) is considered in these equations to correct the conversion and selectivity calculations, accounting for the effect of pressure changes (due to gas expansion and temperature increase) on the flow rate, which is self-consistently calculated in the model at each simulation step.

3. Results and discussion

3.1. Modelled plasma characteristics

The peak power density, pulse duration and energy per pulse implemented in the model, and the response of the calculated maximum reduced electric field, electron density and electron temperature (i.e. at the peak of the pulses) at each applied pressure are summarised in Table 2.

Table 2. Pulse characteristics in the model and calculated maximum electron density (n_e), maximum electron temperature (T_e) and maximum reduced electric field (E/N) at different pressures. The experimentally estimation maximum E/N values are shown in the last column for comparison (the value marked with * was estimated at 3.3 bar)

[22]. Experimental assessment of E/N was carried out via the capacitive probe method described in [24], determining the field (E), given by the electric potential (V) across the electrodes divided by the length of the discharge gap (l), and assuming a constant neutral species density N = 2.66 × 10^{19} cm^{-3}.

Pressure (bar)	Pulse characteristics			n_e max (cm^{-3})	T_e max (eV)	E/N max (Td)	Measured E/N max (Td)
	Peak power density (MW . cm^{-3})	Duration (ns)	Energy (mJ)				
1	183.2	18.0	19.2	1.0x10^{16}	4.4	345.6	244
2	205.3	14.2	17.1	8.2x10^{15}	4.1	280.6	163
3	213.1	12.3	15.3	7.0x10^{15}	3.9	247.0	102*
4	239.2	10.7	15.0	6.1x10^{15}	3.7	215.4	
5	270.4	9.36	14.8	4.5x10^{15}	3.6	181.9	70

As the duration of the pulses decreases with rising pressure, less energy per pulse is channelled into the reactor, despite the higher peak power density. This observation is consistent with the experimental results published by Delikonstantis et al. for NPD CH_4 plasmas in the 1 to 5 bar pressure range [22], and it is also in line with modelled trends for other pressurised NPD systems [14], [23], [26], [27]. The calculated response of the reduced electric field (and in turn that of the electron temperature) to the power pulses exhibits pulsed behaviour (top and middle plots in Figure 1), with peaks registered in the beginning of each power density pulse. This observation is as expected since the model applies the power input to compute the electric field, which is transferred to BOLSIG+ for EEDF and electron temperature calculations. The latter governs the energy of the electrons in the plasma which becomes high during the pulses, triggering electron impact dissociation of CH_4 molecules upon power application. As the reduced electric field is inversely proportional to the density of gas-phase species, the modelled maximum values of E/N are reduced as the pressure is increased. This is also observed in the experimental estimations of E/N (see last column in Table 2). The discrepancy in the absolute values of modelled versus experimental E/N is likely due to the nanoscale duration of the pulses and deposition of solid carbon on the electrodes, rendering accurate experimental assessment of the electric field very challenging and resulting in delayed (i.e. lower) measurements. On the other hand, the modelled E/N is also subject to uncertainties due to the approximation of spatial independence, inherent to the calculations in a 0D chemical kinetics model.

As illustrated in Figure 1 (bottom plot), the model shows that the electron density also peaks with the power pulses along the residence time, with the maximum varying from 4.5 x 10^{15} cm^{-3} at 5 bar to 1.0 x 10^{16} cm^{-3} at 1 bar (see Table 2). In line with the pulsed power density, these peaks are intense but short lived, hence both electron density and temperature fall to negligible levels (1.0 x 10^{9} cm^{-3} and 0.08 eV) in the absence of power between the pulses. Thus, electron impact processes are halted, and recombination reactions become dominant in the interpulse periods (i.e. in the afterglows). The large increase in the peak of electron density over the second pulse (compared to the first pulse), i.e. at 1.9 ms, is due to the increase in the

reduced electric field, as the gas temperature in the system rises, as discussed also in our previous study [16].

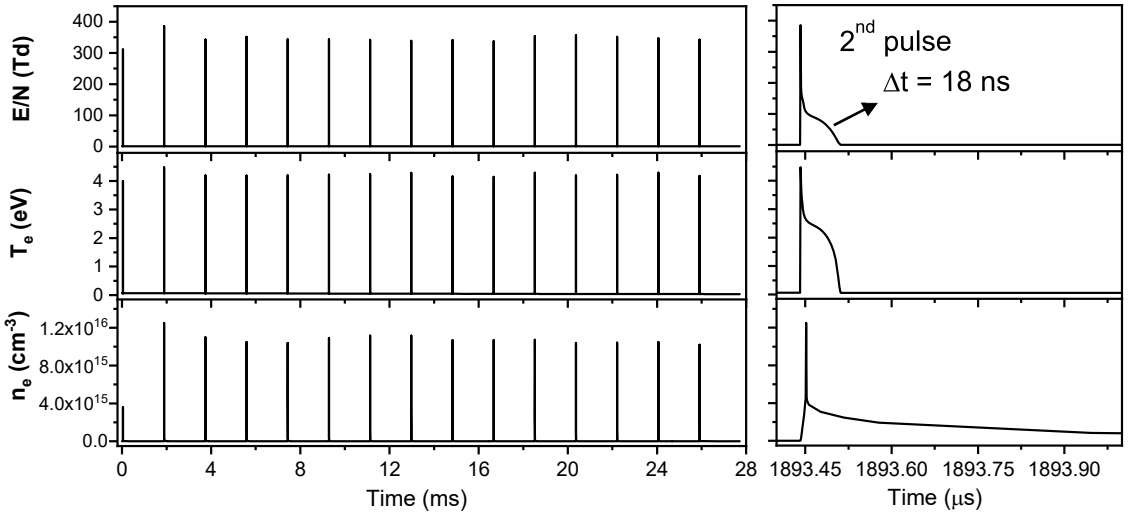

Figure 1. Calculated temporal profile of the reduced electric field E/N (top) and the ensuing responses of the electron temperature, T_e (middle) and electron density, n_e (bottom) (a) in the entire residence time (27.9 ms) and (b) over the second pulse and the beginning of the following afterglow. These calculations were performed at 1 bar.

3.2. Modelled species densities

Consistent with the calculated E/N, electron temperature and density, the density profiles of all species studied in our model also exhibit pulsed behaviour. The density profiles of the main species are plotted in Figure 2. The density of all stable molecules, i.e. CH_4, H_2, C_2H_2 and C_2H_4, fall with the concomitant power pulses, while the radical and ion species pulses exhibit a sharp and rapid peak. These trends are reverted when the pulse ends, i.e. stable species see a steep density increase, whilst those of the radicals and ions sharply drop, and more gradual and slower variations are seen in the afterglows.

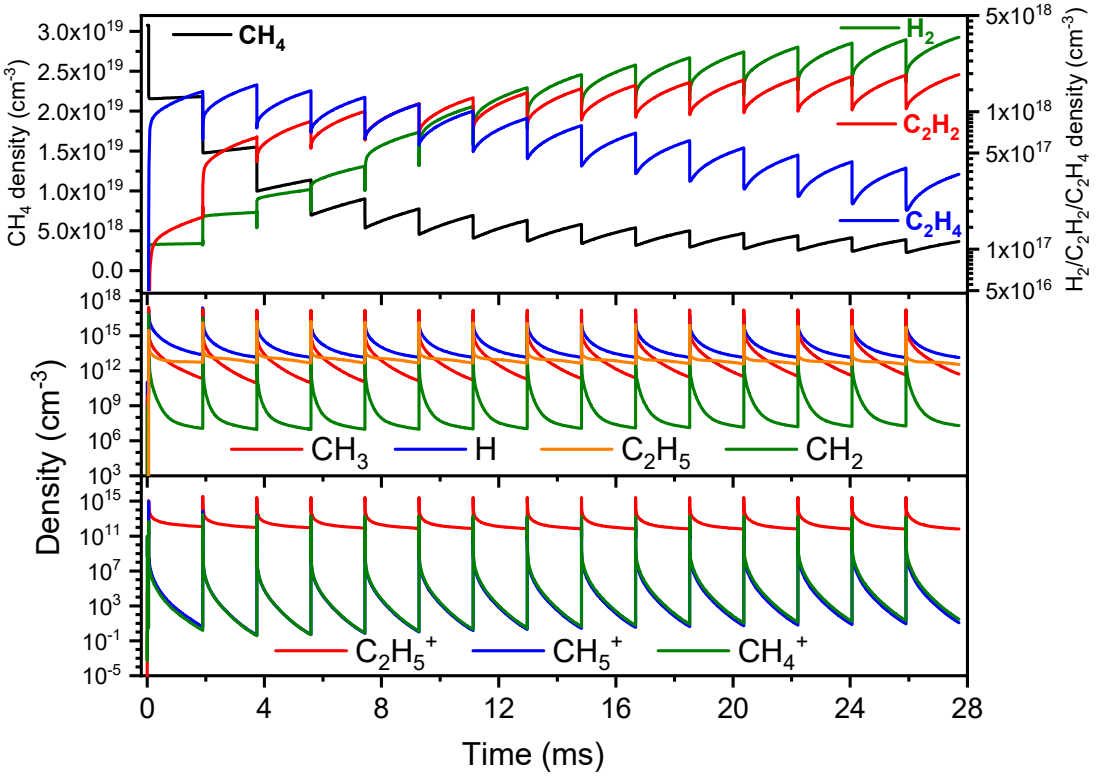

Figure 2. Modelled density profiles of stable molecules with CH_4 being the reactant and H_2, C_2H_2 and C_2H_4 the main gaseous products (top), principal radical species (middle) and main ionic species (bottom) in the simulations. These calculations were performed at 1 bar.

The profiles of the stable molecules (top plot in Figure 2) indicate an overall consumption of CH_4, as the feed molecule is dissociated through electron impact (cf. decrease in density during the pulses) and reformed in the afterglows (exhibiting steady growth) via the CH_3 + H recombination channel. H_2 is the product with highest density in this system, followed by the C_2H_2 and C_2H_4 hydrocarbons. C_2H_6 remains a minor product with much lower densities over the residence time (~ 5 x 10^{16} cm^{-3}). These products also undergo consumption during the pulses (hence the sharp drop in their density profile), however they are reformed in the afterglows, exhibiting a continuous growing density trend as a function of the residence time. The modelled densities of the main radicals and ions (middle and bottom plots in Figure 2) reveal that the order of abundance of these species (during the pulses) is CH_3 > H > C_2H_5 > CH_2 and $C_2H_5^+$ > CH_5^+ > CH_4^+, respectively. The density peaks are reached via a steep rise during the power pulses and are followed by a (also steep) drop to ~ ¾ of the maximum density as the pulse ends. In the afterglows, the decrease decelerates, resulting in the tails seen in all profiles of the radicals and ions.

3.3. Modelled conversion, selectivity and experimental validation

Figure 3 shows the modelled and experimental trends of CH_4 conversion and product selectivity across the 1 to 5 bar pressure range. The results demonstrate that the applied pressure has an important effect on CH_4

conversion and on product selectivity (although more pronounced in the calculated selectivity trends). Both model and experiments see an increase in CH_4 conversion upon increasing pressure, with peak conversion registered at ~ 3 bar (3.3 bar in the experiments). Further pressure increases appear to have a negative impact, as reduced conversions are observed in the 4 to 5 bar range. While lesser in the experiments, this decrease is very pronounced in the modelled results, leading to considerably lower conversions than that registered at 3 bar.

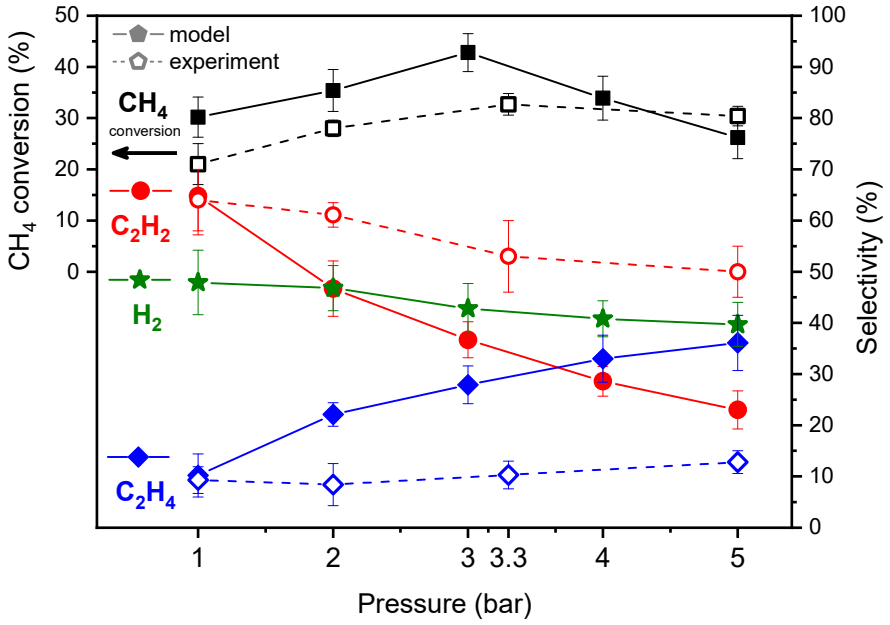

Figure 3. CH_4 conversion and selectivity of H_2, C_2H_2 and C_2H_4. Modelled and experimental results are compared across the 1 to 5 bar pressure range. H_2 selectivity was only assessed in the model. The experiments were carried out at 1, 2, 3.3 and 5 bar and are described in the study by Delikonstantis et al [22], whilst the simulations were run with 1 bar increments.

In terms of selectivity, model and experiments both show C_2H_2 as the main product at 1 bar, followed by H_2 (only modelled selectivity) and C_2H_4. In fact, a remarkably good agreement can be observed at 1 bar and these results tally well with other studies of CH_4 conversion in NPD plasmas [11], [14], [23]. As the pressure is raised, however, model and experiments begin to exhibit discrepancies in the selectivity towards C_2H_2 and C_2H_4. While the C_2H_4 production remains largely unaffected by pressure in the experiments (with selectivity fluctuating around 10%), increased pressures in the model have a strong beneficial effect on C_2H_4 formation. In fact, the model predicts ~ 10% C_2H_4 selectivity at 1 bar (in line with the experiments), growing steadily to 35% at 5 bar. Evidently, the C_2H_2 selectivity sees a concomitant decrease, which is again considerably more accentuated in the model (from 60 to 25%). This trend was also registered in our previous study in CH_4 and H_2 plasmas [16] and in later experimental works by Delikonstantis et al. [11], [23], which reported gains in C_2H_4 selectivity at higher pressures for NOMC in NPD systems. While this discrepancy may signal that the model underestimates the gas temperature at high pressures (in turn leading

to an overestimated ratio between C_2H_4/C_2H_2 selectivity), it may also be an indication that the power inputs in the experiments could have varied with pressure, influencing the average gas temperature, conversion and product distribution. This effect cannot be verified due to unavailability of voltage and current data for these experiments.

Another reason for selectivity discrepancies as a function of pressure may be the effect of soot production, which is widely reported in the experiments, especially in the conditions under study (i.e. in the absence of H_2 in the gas feed), and which is difficult to accurately capture in a 0D model. Albeit detected, the formation of solid particles was not quantified owing to challenges in collecting and measuring the mass of the solids. This model attempted to simulate $C_{(s)}$ formation via stepwise dehydrogenation reactions in the H-Abstraction C_2-Splitting (HACS) channel, i.e. $C_2H_y \rightarrow 2\ C_{(s)} + \frac{y}{2} H_2$ [28]. The results show moderate quantities of $C_{(s)}$ being formed at all pressures, with a maximum concentration of ~ 6% registered at 1 to 3 bar. The model also predicts that the $C_{(s)}$ concentration decreases above 3 bar, with a minimum of ~ 1.5% at 5 bar. This also contributes to lowering the CH_4 conversions above 3 bar. However, this trend in $C_{(s)}$ concentration remains unverified awaiting further experimental validation. Most likely, the lower $C_{(s)}$ quantities predicted upon increased pressure reflect the also lower maximum of the gas temperature attained at higher pressures (as previously shown in our CH_4/H_2 plasmas) [16], which reduces the efficiency of the HACS channels, in turn leading to less $C_{(s)}$ [29]. In future works, this approach should be expanded to account for the influence of surfaces on the HACS mechanism, and to include polymerisation via benzene and acetylene monomer additions, which are also important pathways for soot formation [30], [31].

C_2H_6 was only detected in the model as a minor product with very low selectivity across the studied pressure range, but rising from 0.8% at 1 bar to 2.6% at 5 bar. This selectivity increase is readily ascribed to the $CH_3 + CH_3 + M \rightarrow C_2H_6 + M$ recombination reaction which is enhanced by increasing the applied pressure.

Regarding H_2, this product was not measured in the experiments, thus only the modelled values for selectivity are shown in Figure 3. The H_2 selectivity dwindles slightly as the pressure is increased, falling from 44% at 1 bar to 40% at 5 bar. The decrease is possibly reflected in the C_2H_2 selectivity drop and C_2H_4 selectivity gain (discussed above), as larger quantities of H atoms remain attached to the C_2 hydrocarbon molecules. From an indirect assessment performed via a H balance using the available experimental results [22], the H_2 selectivity does not appear to be pressure dependent in the experiments either, with estimated figures varying between 35 and 45%. Although this H_2 selectivity was obtained via an approximative method (since the experiments do not report the concentrations of C_2H_6 and C_3 species or the composition of the solids produced), this result is generally well aligned with the calculated counterparts. This H_2 selectivity trend suggests that the applied pressure does not affect the rate of H_2 production from CH_4 conversion in NPD plasmas, although direct experimental validation is required to confirm this calculation

result. To corroborate and aid the comprehension of these results, a detailed reaction pathway analysis is presented in section 3.5 below.

Overall, the CH_4 conversion and C_2 selectivity trends in Figure 3 signal reasonable alignment between the model and experiments (especially at 1 bar), which accredits the model's capability to capture the gas-phase kinetics of CH_4 conversion in NPD plasmas.

3.4. Modelled gas temperature and heating dynamics

The temporal evolution of the reaction rates, electron and gas temperatures (self-consistently calculated via the enthalpy variations induced by the processes included in the model, as described in section 2.1 above) was investigated in the 1 to 5 bar pressure range, offering insights into the interplay between temperature, pressure and chemical reactivity. This time-resolved analysis allows for (i) the assessment of the heating dynamics (see Figure 4) and (ii) the study of the CH_4 (and other molecules) dissociation and recombination pathways in this NPD plasma (presented below).

This study has found that vibrational excitation of CH_4 molecules to CH_4 (v1, 3) and CH_4 (v2, 4) does not contribute to CH_4 dissociation, in line with our previous work [16] and other reports on CH_4 conversion [12], [32]–[34], because these excited species undergo nearly instantaneous quenching (~ 50 ns) to ground-state CH_4 via vibrational-translation relaxation. However, unlike in the CH_4/H_2 plasma previously investigated [16], the present model predicts that upon VT relaxation to CH_4 (v4), vibrationally excited CH_4 (v1, 3) and CH_4 (v2) molecules are responsible for over 90% of the heat released into the system in the first three power pulses (see Figure 4).

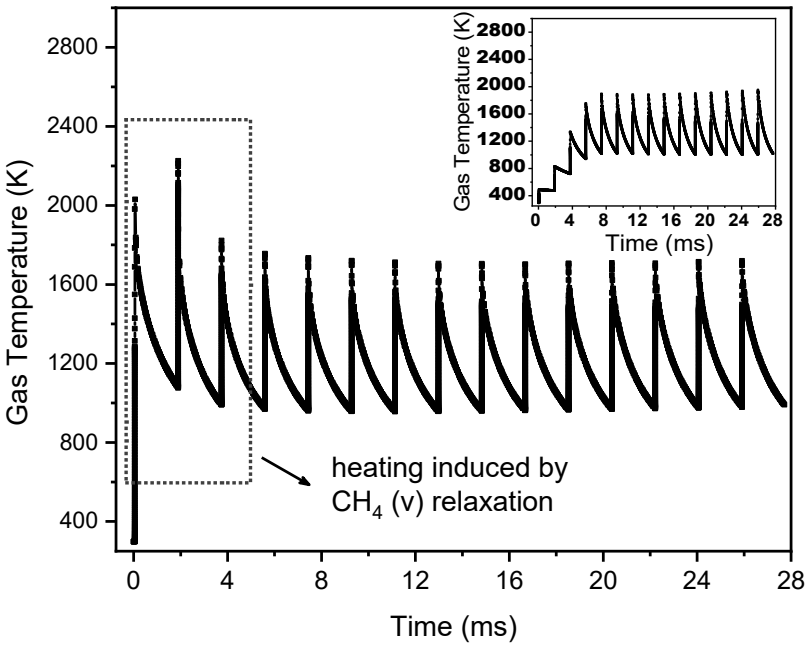

Figure 4. Calculated temperature profile at 1 bar, showing the pulsed evolution of the gas temperature as a function of the residence time. The impact of CH_4 (v) relaxation on the heating dynamics becomes clear by comparison with the inset, which displays a temperature profile calculated in the absence of CH_4 (v) kinetics, highlighting the significant difference in the gas temperature over the first three power pulses.

Four reactions have marked importance in the heat release in the first 4 ms:

1. CH_4 (v3) + CH_4 → CH_4 (v4) + CH_4 ΔH = - 20.45 (kJ mol^{-1})
2. CH_4 (v1) + CH_4 → CH_4 (v4) + CH_4 ΔH = - 19.30 (kJ mol^{-1})
3. CH_4 (v2) + CH_4 → CH_4 (v4) + CH_4 ΔH = - 2.70 (kJ mol^{-1})
4. CH_4 (v3) + CH_4 (v4) → CH_4 (v4) + CH_4 (v4) ΔH = - 20.45 (kJ mol^{-1})

These results suggest that in the absence (and at low densities) of H_2 molecules during the first 4 ms of the simulation (see H_2 density evolution profile in Figure 2), there is no competition between H_2 and CH_4 for electron-impact-driven vibrational excitations, and thus the vibrational levels of CH_4 can be populated to high densities (with a maximum of 4 x 10^{18} cm^{-3}); and upon relaxation, energy is released as heat. This mechanism of energy coupling into gas-phase heating seems to have low efficiency in the presence of H_2, as the model shows that vibrational excitation of H_2 to H_2 (v1) can be up to 16 times more favourable than that of CH_4 to CH_4 (v1, 3) and CH_4 (v2, 4). This is the reason why heating via CH_4 vibrational deexcitation only prevails in the first 4 ms, prior to any significant H_2 production in pure CH_4 NPD plasmas, and does not seem to occur at all when H_2 is present in the gas feed, as discussed in our previous study [16]. Generally, these results indicate that the vibrational excitation-relaxation of H_2 molecules is more important for gas heating than that of CH_4, after these 4 first pulses, with exothermic vibrational-translational (VT) relaxations of excited H_2 accounting for ~ 28% of the heat released to the gas phase at steady state. Also, the model reveals the other two major contributors to gas heating are (i) elastic momentum transfer (~ 35 %) and (ii) CH_3 + H recombination (~ 37 %).

3.5. *Reaction pathway analysis*

Figure 5 presents a reaction diagram network, summarising the mechanisms for H_2 (and C_2 hydrocarbon) production under the modelled conditions.

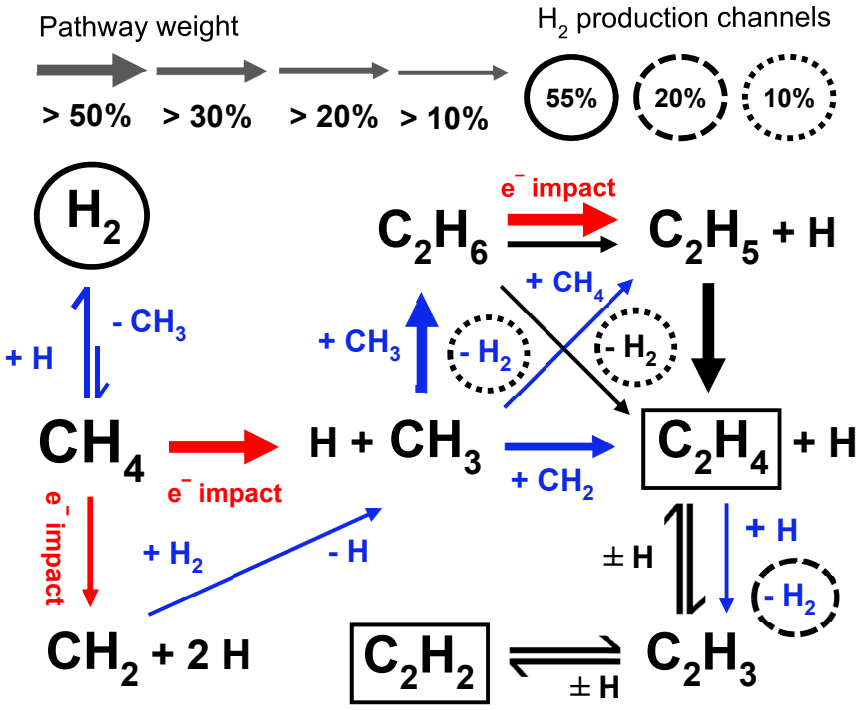

Figure 5. The main reaction pathways involved in the dissociation of CH_4 into H_2 and coupling into C_2 hydrocarbons at steady state. The other H_2 formation channels (involving C_2 hydrocarbons) are also displayed. This analysis is generally valid in the 1 to 5 bar pressure range. The respective percentage contributions are indicated by the circles and the thickness of each arrow is also related to the percentage efficiency of each process (see legend). Electron impact reactions are indicated by red arrows, heavy particle reactions by blue arrows and molecular dissociations by black arrows. The main hydrocarbon products are shown in boxes. Vibrational kinetics are not shown for clarity.

In this pure CH_4 NPD plasma, the dynamics of CH_4 dissociation and radical recombination to C_2 products largely follow the pathways described by our previously discussed CH_4/H_2 model [16]. In brief, the power pulses give rise to a high density of electrons, which collide with incoming CH_4 molecules, triggering C–H bond cleavage into CH_3 (78.4%) and CH_2 (21.0%) (and H) radicals. The principal avenue for CH_4 splitting occurs via electronic excitation through the CH_4^* (7.9 eV) state, which undergoes immediate dissociation, accounting for over 90% of all C_1 radical formation [35], [36]. In the afterglows, rapid vibrational relaxation and recombination reactions (the latter taking place on the µs timescale) largely govern the gas-phase chemistry, as electron impact processes are halted. CH_4 molecules are formed anew via the CH_3 + H channel, which gains traction with increasing pressure, elucidating the lower CH_4 conversions in the experiments and model at pressures greater than 3 bar.

The CH_3 and CH_2 radicals also recombine upon C–C coupling, thereby generating the first C_2H_6, C_2H_4 and C_2H_5 species in the system via the reactions: (i) $CH_3 + CH_3 \rightarrow C_2H_6$, (ii) $CH_3 + CH_2 \rightarrow C_2H_4 + H$ and (iii) $CH_3 + CH_4 \rightarrow C_2H_5 + H_2$, which account for 22%, 10.5% and 3% of CH_3 radical consumption, respectively, while the CH_3 + H recombination into CH_4 accounts for 64.5% of CH_3 consumption. Akin to the CH_4/H_2

plasma system [16], at the average gas temperatures in the model (> 1000 K), the above radical reactions are followed by stepwise dehydrogenation, eventually leading to C_2H_2 (see Figure 5). The equilibrium of the $C_2H_4 \rightleftharpoons C_2H_3 \pm H \rightleftharpoons C_2H_2$ reactions is regulated by the applied pressure, with C_2H_4 being favoured at pressures greater than 4 bar, whilst C_2H_2 is dominant at lower pressures.

Novel and more noteworthy here are the findings from the kinetics of H_2 production and consumption. At steady state, H_2 is predominantly formed in four reactions, which mainly occur in the afterglows (the respective relative contributions are indicated):

1. $CH_4 + H \rightarrow CH_3 + H_2$ (~ 55%)
2. $C_2H_4 + H \rightarrow C_2H_3 + H_2$ (~ 20%)
3. $CH_4 + CH_3 \rightarrow C_2H_5 + H_2$ (~ 10%)
4. $M + C_2H_6 \rightarrow M + C_2H_4 + H_2$ (~ 10%)

The relative contributions (also shown in Figure 5) amount to 95% of all H_2 produced when the gas temperature stabilises. From the remaining 5%, 4% are due to H atom recombination in the $M + H + H \rightarrow M + H_2$ reaction (where M is any gas species acting as third body). The latter reaction, alongside $M + C_2H_6 \rightarrow M + C_2H_4 + H_2$, are the only two important pressure-dependent mechanisms for H_2 formation. Since the applied pressure affects these two mechanisms in a competing manner (i.e. the dissociation of C_2H_6 is favoured at lower pressures and inhibited at high pressures, while the applied pressure has the opposite effect on H + H recombination, which is a three-body reaction), it is plausible to posit that pressure will not significantly affect H_2 production in this NPD CH_4 plasma. This is in line with the calculated H_2 selectivity (Figure 3 above), which remains mostly unaffected across the pressure range studied.

Conversely, during the power pulses, H_2 is converted, undergoing electronic and vibrational excitation via impact with hot electrons (and ensuing energy transfer to the gas phase) in the following reactions (i) $H_2 + e^- \rightarrow H_2$ (v1, 5) + e^- and (ii) $H_2 + e^- \rightarrow H_2^* + e^- \rightarrow H + H + e^-$, and ionisation via the (iii) $H_2 + e^- \rightarrow H_2^+ + 2\ e^-$ reaction. These constitute the three major loss pathways, accounting for 72%, 18% and 4% of the total H_2 reacting in the pulses. The vibrational promotions create an excitation-deexcitation loop (leading to rapid H_2 (v) relaxation to H_2 via exothermic VT interactions), which results in the steep rises seen immediately after each pulse in the H_2 density profile in Figure 2 and contributes with ~ 28% to the heat maintenance mechanism at steady state, as discussed above. While vibrational excitation does not result in H_2 dissociation, electronic excitation to H_2^* (11.83 eV) promptly induces H_2 splitting (as shown in the second reaction above) and ionisation to H_2^+ leads to ion exchange reactions with H_2 and CH_4 (producing H_3^+, CH_3^+ and CH_5^+), ultimately also contributing to H_2 loss. Combined, these three processes are responsible for ~ 27% of the total energy consumed in the pulses at steady state. The remaining percentage in energy

consumption is composed of elastic collisions (~ 38%), CH_4 excitation, dissociation and ionisation (~ 21%), and excitations, dissociations and ionisations of other molecules (~ 14%).

4. Conclusions

In this work, a time-resolved 0D chemical kinetics model was developed to investigate an NPD plasma with a gas feed of 100% CH_4, and its conversion into H_2 and C_2 hydrocarbons. The model considered the effect of applied pressure on the pulsed power depositions and on various plasma properties, such as the reduced electric field, electron density and electron temperature at different pressures. The gas temperature was calculated self-consistently with time, based on enthalpy changes induced by the chemical reactions included in the model.

The modelled variations in CH_4 conversion and C_2 hydrocarbon product selectivity as a function of applied pressure were compared with experimental results from literature for pure CH_4 in a coaxial reactor under NPD conditions. Model and experiments are overall well aligned at 1 bar, however the modelled selectivity towards C_2H_2 and C_2H_4 begins to deviate from those measured in the experiments at higher pressures. The discrepancies can be attributed to possible underestimations of gas temperature in the model and also to the difficulties in modelling soot formation which is widely seen in the experiments.

The simulations have shed light on the gas-phase dynamics of CH_4 dissociation and reforming following a mechanistic analysis, which elucidates the reaction pathways involved in the production of H_2 and C_2 species. Analogously, the model predicts that H_2 formation is not affected by the applied pressure (with calculated selectivity around ~ 42% from 1 to 5 bar), as most reactions leading to H_2 are pressure independent, and the two pressure-dependent routes are compensatory. Further, the model also shows that vibrationally excited CH_4 and H_2 molecules play an essential role in coupling the energy from the power pulses into gas-phase heating in this CH_4 NPD plasma.

Prospective work plans to investigate an expanded approach to capture soot formation in the model by including aromatic and linear polymerisation routes and the effect of surfaces on the nucleation of solid particles from the various gas-phase reactants present in the plasma. It would also be of interest to carry out spectroscopic measurements in the plasma region to provide further experimental data for model validation.

5. Acknowledgements

We gratefully acknowledge financial support by the Flemish Government through the Moonshot cSBO project “Power-to-Olefins” (P2O; HBC.2020.2620) and funding from the Independent Research Fund Denmark (project nr. 0217-00231B).

6. References

[1] L. Fulcheri, V. J. Rohani, E. Wyse, N. Hardman, and E. Dames, “An energy-efficient plasma methane pyrolysis process for high yields of carbon black and hydrogen,” *Int. J. Hydrogen Energy*, vol. 48, no. 8, pp. 2920–2928, 2023, doi: 10.1016/j.ijhydene.2022.10.144.

[2] M. Scapinello, E. Delikonstantis, and G. D. Stefanidis, “The panorama of plasma-assisted non-oxidative methane reforming,” *Chemical Engineering and Processing: Process Intensification*, vol. 117. Elsevier B.V., pp. 120–140, 2017, doi: 10.1016/j.cep.2017.03.024.

[3] J. Feng *et al.*, “Plasma-Assisted Reforming of Methane,” *Adv. Sci.*, vol. 9, no. 34, p. 2203221, Dec. 2022, doi: 10.1002/advs.202203221.

[4] N. Budhraja, A. Pal, and R. S. Mishra, “Plasma reforming for hydrogen production: Pathways, reactors and storage,” *Int. J. Hydrogen Energy*, vol. 48, no. 7, pp. 2467–2482, 2023, doi: 10.1016/j.ijhydene.2022.10.143.

[5] A. Bogaerts and E. C. Neyts, “Plasma Technology: An Emerging Technology for Energy Storage,” *ACS Energy Letters*, vol. 3, no. 4. pp. 1013–1027, 2018, doi: 10.1021/acsenergylett.8b00184.

[6] S. Liu, L. R. Winter, and J. G. Chen, “Review of Plasma-Assisted Catalysis for Selective Generation of Oxygenates from CO_2 and CH_4,” *ACS Catal.*, vol. 10, no. 4, pp. 2855–2871, 2020, doi: 10.1021/acscatal.9b04811.

[7] H. Chen, Y. Mu, S. Xu, S. Xu, C. Hardacre, and X. Fan, “Recent advances in non-thermal plasma (NTP) catalysis towards C_1 chemistry,” *Chinese Journal of Chemical Engineering*, vol. 28, no. 8. pp. 2010–2021, 2020, doi: 10.1016/j.cjche.2020.05.027.

[8] N. Sánchez-Bastardo, R. Schlögl, and H. Ruland, “Methane Pyrolysis for Zero-Emission Hydrogen Production: A Potential Bridge Technology from Fossil Fuels to a Renewable and Sustainable Hydrogen Economy,” *Ind. Eng. Chem. Res.*, vol. 60, no. 32, pp. 11855–11881, 2021, doi: 10.1021/acs.iecr.1c01679.

[9] S. Heijkers, M. Aghaei, and A. Bogaerts, “Plasma-Based CH_4 Conversion into Higher Hydrocarbons and H2: Modeling to Reveal the Reaction Mechanisms of Different Plasma Sources,” *J. Phys. Chem. C*, vol. 124, no. 13, pp. 7016–7030, 2020, doi: 10.1021/acs.jpcc.0c00082.

[10] M. Hrabovsky *et al.*, “Steam Plasma Methane Reforming for Hydrogen Production,” *Plasma Chem. Plasma Process.*, vol. 38, no. 4, pp. 743–758, 2018, doi: 10.1007/s11090-018-9891-5.

[11] E. Delikonstantis, M. Scapinello, O. Van Geenhoven, and G. D. Stefanidis, “Nanosecond pulsed discharge-driven non-oxidative methane coupling in a plate-to-plate electrode configuration plasma reactor,” *Chem. Eng. J.*, vol. 380, no. August 2019, p. 122477, 2020, doi: 10.1016/j.cej.2019.122477.

[12] P. D. G. Maqueo, M. Maier, M. D. G. Evans, S. Coulombe, and J. M. Bergthorson, “Regimes of an atmospheric pressure nanosecond repetitively pulsed discharge for methane partial oxidation,” *J. Phys. D. Appl. Phys.*, vol. 51, no. 13, 2018, doi: 10.1088/1361-6463/aab0cb.

[13] D. L. Kuznetsov, V. V. Uvarin, and I. E. Filatov, “Plasma chemical conversion of methane by pulsed electron beams and non-self-sustained discharges,” *J. Phys. D. Appl. Phys.*, vol. 54, no. 43, 2021, doi: 10.1088/1361-6463/ac17b2.

[14] M. Scapinello, E. Delikonstantis, and G. D. Stefanidis, “A study on the reaction mechanism of non-oxidative methane coupling in a nanosecond pulsed discharge reactor using isotope analysis,” *Chem. Eng. J.*, vol. 360, pp. 64–74, Mar. 2019, doi: 10.1016/j.cej.2018.11.161.

[15] S. Kado, K. Urasaki, Y. Sekine, K. Fujimoto, T. Nozaki, and K. Okazaki, “Reaction mechanism of methane activation using non-equilibrium pulsed discharge at room temperature,” *Fuel*, vol. 82, no. 18, pp. 2291–2297, Dec. 2003, doi: 10.1016/S0016-2361(03)00163-7.

[16] E. Morais, E. Delikonstantis, M. Scapinello, G. Smith, G. D. Stefanidis, and A. Bogaerts, “Methane coupling in nanosecond pulsed plasmas: Correlation between temperature and pressure and effects on product selectivity,” *Chem. Eng. J.*, vol. 462, no. February, p. 142227, 2023, doi: 10.1016/j.cej.2023.142227.

[17] T. Kozák and A. Bogaerts, “Evaluation of the energy efficiency of CO_2 conversion in microwave discharges using a reaction kinetics model,” *Plasma Sources Sci. Technol.*, vol. 24, no. 1, 2015, doi: 10.1088/0963-0252/24/1/015024.

[18] L. Pancheshnyi, Sergey ; Eismann, Benjamin ; Hagelaar, Gerjan ; Pitchford, “ZDPlasKin: a new tool for plasmachemical simulations,” 2008, [Online]. Available: http://www.laplace.univ-tlse.fr.

[19] A. Berthelot, S. Kolev, and A. Bogaerts, “Different Pressure Regimes of a Surface-Wave Discharge in Argon: a Modeling Investigation,” *Proc. ninth Int. Work. Microw. Discharges Fundam. Apllications*, pp. 58–62, 2015, Accessed: Sep. 28, 2022. [Online]. Available: www.comsol.com.

[20] D. G. Friend, J. F. Ely, and H. Ingham, “Thermophysical Properties of Methane,” *J. Phys. Chem. Ref. Data*, vol. 18, no. 2, pp. 583–638, Apr. 1989, doi: 10.1063/1.555828.

[21] G. J. M. Hagelaar and L. C. Pitchford, "Solving the Boltzmann equation to obtain electron transport coefficients and rate coefficients for fluid models," *Plasma Sources Sci. Technol.*, vol. 14, no. 4, pp. 722–733, 2005, doi: 10.1088/0963-0252/14/4/011.
[22] M. Scapinello, E. Delikonstantis, and G. D. Stefanidis, "Direct methane-to-ethylene conversion in a nanosecond pulsed discharge," *Fuel*, vol. 222, no. December 2017, pp. 705–710, 2018, doi: 10.1016/j.fuel.2018.03.017.
[23] E. Delikonstantis, M. Scapinello, and G. D. Stefanidis, "Low energy cost conversion of methane to ethylene in a hybrid plasma-catalytic reactor system," *Fuel Process. Technol.*, vol. 176, pp. 33–42, Jul. 2018, doi: 10.1016/J.FUPROC.2018.03.011.
[24] R. Lotfalipour, A. M. Ghorbanzadeh, and A. Mahdian, "Methane conversion by repetitive nanosecond pulsed plasma," *J. Phys. D. Appl. Phys.*, vol. 47, no. 36, 2014, doi: 10.1088/0022-3727/47/36/365201.
[25] M. Scapinello, L. M. Martini, G. Dilecce, and P. Tosi, "Conversion of CH_4/CO_2 by a nanosecond repetitively pulsed discharge," *J. Phys. D. Appl. Phys.*, vol. 49, no. 7, 2016, doi: 10.1088/0022-3727/49/7/075602.
[26] M. S. Moss, K. Yanallah, R. W. K. Allen, and F. Pontiga, "An investigation of CO_2 splitting using nanosecond pulsed corona discharge: Effect of argon addition on CO_2 conversion and energy efficiency," *Plasma Sources Sci. Technol.*, vol. 26, no. 3, 2017, doi: 10.1088/1361-6595/aa5b1d.
[27] A. Lo *et al.*, "Streamer-to-spark transition initiated by a nanosecond overvoltage pulsed discharge in air," *Plasma Sources Sci. Technol.*, vol. 26, no. 4, 2017, doi: 10.1088/1361-6595/aa5c78.
[28] F. Serse *et al.*, "A comprehensive kinetic framework for solid carbon deposition and hydrogen production from the pyrolysis of light hydrocarbons streams," *Carbon Trends*, vol. 11, no. February, p. 100263, 2023, doi: 10.1016/j.cartre.2023.100263.
[29] A. Holmen, O. Olsvik, and O. A. Rokstad, "Pyrolysis of natural gas: chemistry and process concepts," *Fuel Process. Technol.*, vol. 42, no. 2–3, pp. 249–267, 1995, doi: 10.1016/0378-3820(94)00109-7.
[30] C. Saggese *et al.*, "Kinetic modeling study of polycyclic aromatic hydrocarbons and soot formation in acetylene pyrolysis," *Energy and Fuels*, vol. 28, no. 2, pp. 1489–1501, 2014, doi: 10.1021/ef402048q.
[31] S. Ravasio and C. Cavallotti, "Analysis of reactivity and energy efficiency of methane conversion through non thermal plasmas," *Chem. Eng. Sci.*, vol. 84, pp. 580–590, Dec. 2012, doi: 10.1016/j.ces.2012.09.012.
[32] P. A. Maitre, M. S. Bieniek, and P. N. Kechagiopoulos, "Modelling excited species and their role on kinetic pathways in the non-oxidative coupling of methane by dielectric barrier discharge," *Chem. Eng. Sci.*, vol. 234, Apr. 2021, doi: 10.1016/j.ces.2020.116399.
[33] T. Butterworth *et al.*, "Plasma induced vibrational excitation of CH_4 - A window to its mode selective processing," *Plasma Sources Sci. Technol.*, vol. 29, no. 9, 2020, doi: 10.1088/1361-6595/aba1c9.
[34] N. Pourali, V. Hessel, and E. V. Rebrov, "The Effects of Pulse Shape on the Selectivity and Production Rate in Non-oxidative Coupling of Methane by a Micro-DBD Reactor," *Plasma Chem. Plasma Process.*, vol. 42, no. 3, pp. 619–640, 2022, doi: 10.1007/s11090-022-10242-6.
[35] B. Huang, C. Zhang, H. Sun, D. A. Sorokin, V. F. Tarasenko, and T. Shao, "Enhancement of hydrogen radical density in atmospheric pressure plasma jet by a burst of nanosecond pulses at 1 MHz," *Plasma Sources Sci. Technol.*, vol. 31, no. 2, 2022, doi: 10.1088/1361-6595/ac3e3e.
[36] B. Huang, C. Zhang, H. Bai, S. Zhang, K. (Ken) Ostrikov, and T. Shao, "Energy pooling mechanism for catalyst-free methane activation in nanosecond pulsed non-thermal plasmas," *Chem. Eng. J.*, vol. 396, 2020, doi: 10.1016/j.cej.2020.125185.

Tables

Table 1. Species considered in the model.

Stable molecules	Radicals	Ions and electrons	Excited molecules
CH_4 H_2 C_2H_2 C_2H_4 C_2H_6 C_3H_6 C_3H_8 C_4H_{10} $C_{(s)}$	C C_2 C_3 H CH_3 CH_2 CH C_2H C_2H_3 C_2H_5 C_3H_5 C_3H_7 C_4H_9	H^+ H_2^+ H_3^+ C^+ C_2^+ CH^+ CH_2^+ CH_3^+ CH_4^+ CH_5^+ C_2H^+ $C_2H_2^+$ $C_2H_3^+$ $C_2H_4^+$ $C_2H_5^+$ $C_2H_6^+$ H^- CH^- CH_2^- electrons	Vibrational: H_2 (v = 1…14) CH_4 (v = 1…4) Electronic: H_2* and CH_4*

Table 2. Pulse characteristics in the model and calculated maximum electron density (n_e), maximum electron temperature (T_e) and maximum reduced electric field (E/N) at different pressures. The experimentally estimation

maximum E/N values are shown in the last column for comparison (the value marked with * was estimated at 3.3 bar) [22]. Experimental assessment of E/N was carried out via the capacitive probe method described in [24], determining the field (E), given by the electric potential (V) across the electrodes divided by the length of the discharge gap (l), and assuming a constant neutral species density $N = 2.66 \times 10^{19}$ cm^{-3}.

Pressure (bar)	Pulse characteristics			n_e max (cm^{-3})	T_e max (eV)	E/N max (Td)	Measured E/N max (Td)
	Peak power density (MW cm^{-3})	Duration (ns)	Energy (mJ)				
1	183.2	18.0	19.2	$1.2\text{x}10^{16}$	4.4	345.6	244
2	205.3	14.2	17.1	$8.2\text{x}10^{15}$	4.1	280.6	163
3	213.1	12.3	15.3	$7.0\text{x}10^{15}$	3.9	247.0	102*
4	239.2	10.7	15.0	$6.1\text{x}10^{15}$	3.7	215.4	
5	270.4	9.36	14.8	$4.5\text{x}10^{15}$	3.6	181.9	70

Figures

Figure 1. Calculated temporal profile of the reduced electric field E/N (top) and the ensuing responses of the electron temperature, T_e (middle) and electron density, n_e (bottom) (a) in the entire residence time (27.9 ms) and (b) over the second pulse and the beginning of the following afterglow. These calculations were performed at 1 bar.

Figure 2. Modelled density profiles of stable molecules with CH_4 being the reactant and H_2, C_2H_2 and C_2H_4 the main gaseous products (top), principal radical species (middle) and main ionic species (bottom) in the simulations. These calculations were performed at 1 bar.

Figure 3. CH_4 conversion and selectivity of H_2, C_2H_2 and C_2H_4. Modelled and experimental results are compared across the 1 to 5 bar pressure range. H_2 selectivity was only assessed in the model. The experiments were carried out at 1, 2, 3.3 and 5 bar and are described in the study by Delikonstantis et al [22], whilst the simulations were run with 1 bar increments.

Figure 4. Calculated temperature profile at 1 bar, showing the pulsed evolution of the gas temperature as a function of the residence time. The impact of CH_4 (v) relaxation on the heating dynamics becomes clear by comparison with the inset, which displays a temperature profile calculated in the absence of CH_4 (v) kinetics, highlighting the significant difference in the gas temperature over the first three power pulses.

Figure 5. The main reaction pathways involved in the dissociation of CH_4 into H_2 and coupling into C_2 hydrocarbons at steady state. The other H_2 formation channels (involving C_2 hydrocarbons) are also displayed. This analysis is generally valid in the 1 to 5 bar pressure range. The respective percentage contributions are indicated by the circles and the thickness of each arrow is also related to the percentage efficiency of each process (see legend). Electron impact reactions are indicated by red arrows, heavy particle reactions by blue arrows and molecular dissociations by black arrows. The main hydrocarbon products are shown in boxes. Vibrational kinetics are not shown for clarity.